Research Article

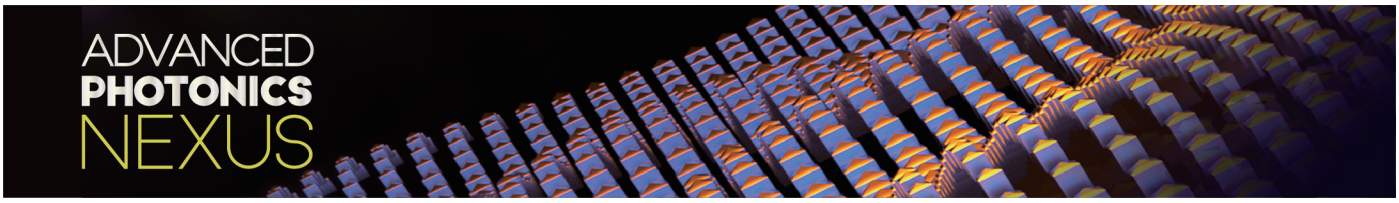

Extremely efficient terahertz second-harmonic generation from organic crystals

Hang Zhao,[a,b,†] Yong Tan,[c,d,e,†] Chen Wang,[c] Ming Liu,[a,b] Yongzheng Wen,[c,*] Yuejin Zhao,[a,b,f,*] and Ji Zhou[c,*]

[a]Beijing Institute of Technology, School of Optics and Photonics, Beijing Key Laboratory for Precision Optoelectronic Measurement Instrument and Technology, Beijing, China
[b]Yangtze Delta Region Academy of Beijing Institute of Technology, Jiaxing, China
[c]Tsinghua University, School of Materials Science and Engineering, State Key Laboratory of New Ceramics and Fine Processing, Beijing, China
[d]Research Center for Metamaterials, Wuzhen Laboratory, Jiaxing, China
[e]Yangtze Delta Region Institute of Tsinghua University, Advanced Ceramic Materials and Devices Research Center, Jiaxing, China
[f]Beijing Broad Hengtong Technology Development Co. Ltd., Beijing, China

Abstract. Achieving efficient and intense second-harmonic generation (SHG) in the terahertz (THz) spectrum holds great potential for a wide range of technical applications, including THz nonlinear functional devices, wireless communications, and data processing and storage. However, the current research on THz harmonic emission primarily focuses on inorganic materials, which often offers challenges in achieving both efficient and broadband SHG. Herein, the remarkable efficiency of organic materials in producing THz harmonics is studied and demonstrated, thereby opening up a new avenue for searching candidates for frequency-doubling devices in the THz band. By utilizing DAST, DSTMS, and OH1 crystals, we showcase their superior frequency conversion capabilities when pumped by the narrowband THz pulses centered at 2.4, 1.6, and 0.8 THz. The SHG spans a high-frequency THz domain of 4.8 THz, achieving an unprecedented conversion efficiency of ~1.21% while maintaining a perturbative nonlinear response. The highly efficient SHG of these materials is theoretically analyzed by considering the combined effects of dispersion, phonon absorption, polarization, and the nonlinear susceptibility of organic crystals. This work presents a promising platform for efficient THz frequency conversion and generation across a wide range of frequencies, offering new opportunities for novel nonlinear THz applications in next-generation electronics and optics.

Keywords: terahertz; organic crystal; second-harmonic generation.

Received Mar. 6, 2024; revised manuscript received Apr. 23, 2024; accepted for publication Jun. 3, 2024; published online Jun. 24, 2024.

[DOI: 10.1117/1.APN.3.4.046007]

1 Introduction

Nonlinear optics explores the nature and laws of the interaction between light and matter and provides an important foundation for a wide range of scientific disciplines and practical applications.[1–5] The spectral boundary between electrons and optics, once known as the "THz gap," appears to be a missing component in the well-established field of nonlinear optics. Extensive research has explored various methods of combining photonics with terahertz (THz) technology, including frequency downconversion techniques, such as optical rectification, difference frequency generation, and air filamentation.[6–11] However, studies on frequency upconversion using second-harmonic generation (SHG) or high-order harmonic radiation to bridge optoelectronics and THz technology are relatively scarce. Current research in THz optical nonlinearity primarily focuses on semiconductors and Dirac semimetals.[12–20] The carriers in the majority of such materials are accelerated symmetrically with respect to the direction of an incident THz field, which leads to nonlinear optical responses that can be described by odd-order electrical susceptibility, where THz odd-order harmonic generation has recently been demonstrated.[12,19,20] On the other hand, the nonlinear processes related to second-order susceptibility, such as optical parametric oscillation and SHG, also have

*Address all correspondence to Yongzheng Wen, wenyzheng@tsinghua.edu.cn; Yuejin Zhao, yjzhao@bit.edu.cn; Ji Zhou, zhouji@tsinghua.edu.cn

†These authors contributed equally to this work.

development potential and are expected to advance various technologies, such as THz nonlinear functional devices, wireless communications, data processing and storage, and radar-based systems.[21–26] Unfortunately, the scarcity of suitable second-order nonlinear materials for the THz spectrum has hindered the exploration of THz nonlinear processes.

Very few pioneering studies on THz SHG have focused primarily on inorganic materials. In earlier studies, researchers have demonstrated that the THz SHG process can arise from the inherent second-order susceptibility of lattice resonance in gallium arsenide (GaAs) and lithium tantalate ($LiTaO_3$)[27] or from the asymmetric electronic response caused by artificial quantum wells.[28] However, due to the weak inherent nonlinearities of materials, the conversion efficiency of these works is generally low.[27,28] In recent years, superconductors have shown promising prospects in achieving efficient SHG due to the dynamical symmetry breaking caused by the lightwave acceleration of supercurrent at cryogenic temperatures.[29] But this solution imposes strict temperature requirements, and the operating frequency band is also limited to a narrowband by the energy gap of the material.[29] The latest research indicates that metamaterials leverage artificially designed resonant structures to enhance nonlinear Thomson scattering, generating SHG at room temperature.[30] Nevertheless, due to limitations such as extremely thin effective thickness in nanometers and low saturation threshold, it is difficult to further improve the conversion efficiency of this metamaterial scheme.[30] In addition, for advanced platforms of superconductors and metamaterials,[29,30] their operations are limited at several specific frequencies, typically below 1 THz, which are also unfavorable for most potential applications. In fact, achieving highly efficient SHG for THz waves over a wider frequency range remains challenging.

On the other hand, organic crystal materials offer high nonlinear coefficients, making them attractive for various photonics techniques.[31,32] To achieve a macroscopic second-order nonlinear optical response, the asymmetric nonlinear optical chromophores in organic crystals have to be distributed non-centrosymmetrically,[33,34] making organic crystals excellent materials for THz sources, such as 4-N, N-dimethylamino-4′-N′-methyl-stilbazolium tosylate (DAST), 4-N,N-dimethylamino-4′-N′-methyl-stilbazolium 2,4,6-trimethylbenzenesulfonate (DSTMS), and 2-(3-(4-hydroxystyryl)-5,5-dimethylcyclohex-2-enylidene) malononitrile (OH1), which are currently considered to be usable strong broadband THz sources and have even been preliminarily commercialized.[9,10,35–37] Recently, these organic crystals have been confirmed as excellent second-harmonic generators in the near-infrared spectrum.[38] Given their strong nonlinearity in the infrared to THz frequency range, we anticipate that these organic materials may become promising candidates for SHG across the entire THz band.

In this study, we demonstrate THz SHG in organic materials with record-breaking conversion efficiency and broad bandwidth. We directly excited three organic crystals, namely, DAST, DSTMS, and OH1, using THz pulses with frequencies of 2.4, 1.6, and 0.8 THz, respectively. Remarkably, we achieved highly efficient SHG over a wide frequency range at room temperature. The field conversion efficiencies of SHG at the high frequency of 4.8 THz from DAST and DSTMS crystals reached over 1%, exceeding all previous reports.[27–30] Importantly, unlike semiconductors, we observed no electric field saturation of SHG as the energy of the THz pump pulse increased, indicating that organic crystals are expected to produce extremely strong harmonic pulses. To evaluate the frequency-doubling capability of these materials, we further investigated the SHG process from the perspectives of dispersion, photon absorption, polarization, and second-order nonlinear susceptibility. Our findings suggest that organic crystals hold great prospects as THz frequency-doubling devices. The proposed THz SHG scheme offers several advantages, including a convenient experimental setup, a wide operating frequency range, and high conversion efficiency. This research provides an excellent platform for the development of THz nonlinear functional devices.

2 Results

2.1 THz SHG from Organic Crystals

Our experiment, as shown in Fig. 1(a), is designed to observe THz harmonics in crystals using strong-field THz time-domain spectroscopy (see Appendix Sec. 4.1 and Supplementary Material for detailed information about the experimental system). Narrowband, multicycle quasi-monochromatic pulses with specific fundamental frequencies of 2.4, 1.6, or 0.8 THz are used to excite substrate-free organic crystals DAST, DSTMS, and OH1. Second harmonics are generated due to the strong second-order nonlinearities and are then filtered at a frequency of 4.8, 3.2, or 1.6 THz and measured using an electro-optical sampling (EOS) device.[39] All measurements are performed at room temperature in a nitrogen atmosphere. The bottom panels of Figs. 1(b)–1(d) display the measured incident THz time-domain waveforms, along with the corresponding peak electric field strengths of 210.3, 78.6, and 23.5 kV/cm, for frequencies of 2.4, 1.6, and 0.8 THz, respectively. We pumped DAST, DSTMS, and OH1 crystals with thicknesses of 300, 300, and 500 μm, respectively, using pulses of these three frequencies and measured the generated second-harmonic time-domain signals, as shown in Fig. S3 in the Supplementary Material. The corresponding THz second-order harmonic spectra are shown in Figs. 1(e)–1(g). It is evident that all three crystals are capable of efficiently generating second-harmonic radiation, although the optimal operating frequency differs for each crystal. Specifically, for THz pulses with pump frequencies of 2.4, 1.6, and 0.8, the DAST, DSTMS, and OH1 crystals exhibit strong harmonic generation capabilities, with clear and visible second-harmonic waveforms and maximum electric fields of 2545, 405, and 11.4 V/cm, respectively, as shown in the upper panels of Figs. 1(b)–1(d). The stability measurement and error evaluation of SHG signals are described in Sec. IV of the Supplementary Material.

2.2 Dependence of SHG on the Incident Electric Field

We examined the relationship between the electric field strength of SHG of different crystals and the fundamental electric field of 2.4, 1.6, and 0.8 THz, as shown in Figs. 2(a)–2(c). The dependence of SHG on field strength can be accurately described by a power law of $|E_{2f}| \propto |E_f|^2$ with respect to the fundamental field strength, indicating a second-order nonlinear response, as anticipated.[40] Notably, this study extends the range of SHG to a high-frequency THz range of 4.8 THz, as shown in Fig. 2(a). The DAST crystal exhibits a high nonlinear field conversion efficiency ($|E_{2f}|/|E_f|$) of 1.21% [the corresponding intensity conversion efficiency (I_{2f}/I_f) is 1.46×10^{-4}], while the DSTMS crystal has a conversion efficiency of 1.08% (the corresponding intensity conversion efficiency is 1.17×10^{-4}),

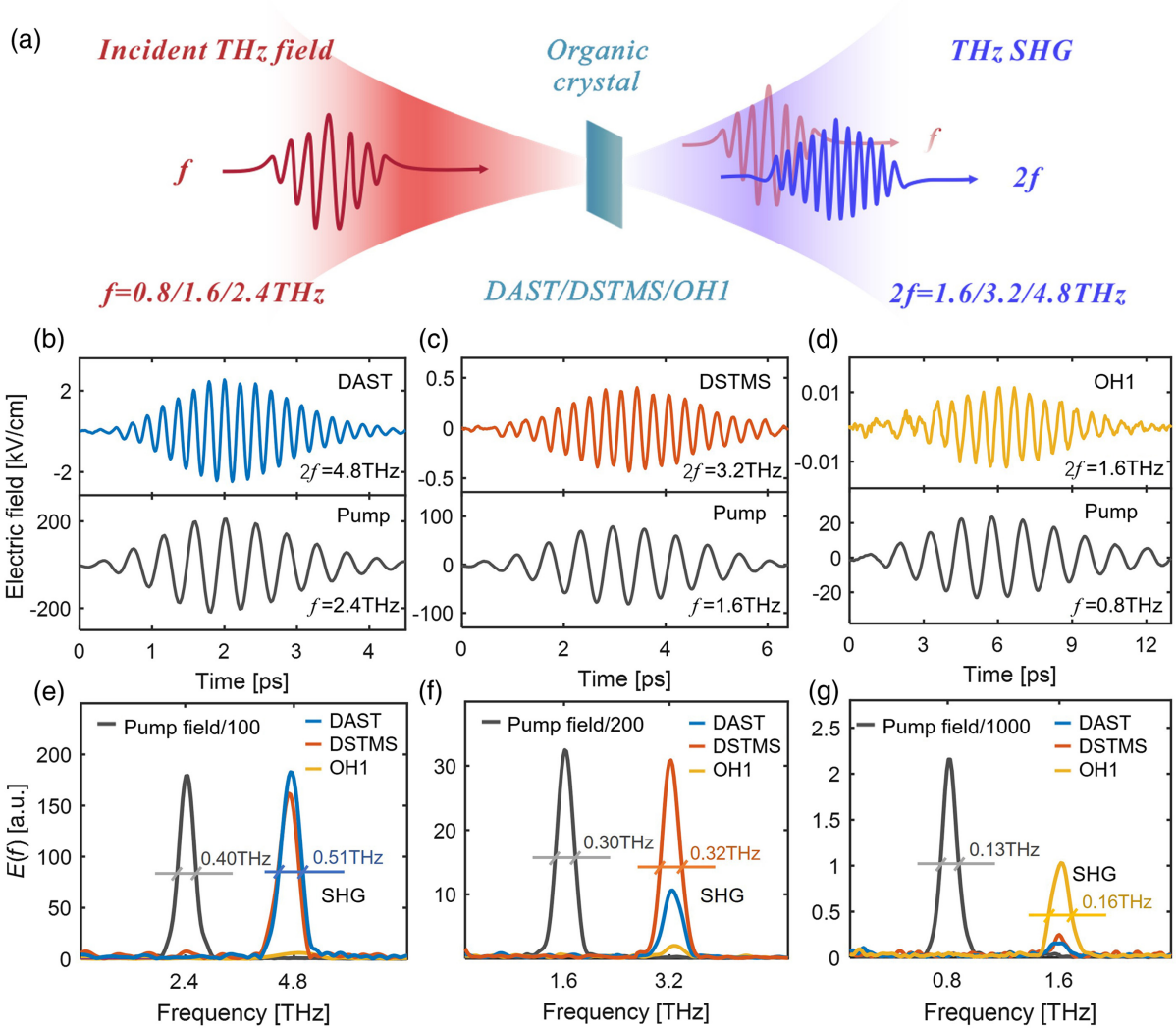

Fig. 1 The THz SHG from organic crystals. (a) Schematic of the experiment. (b) The time-domain waveform of THz SHG from a DAST crystal (upper panel) and the corresponding THz pump waveform with a fundamental frequency of 2.4 THz (lower panel). (c) The time-domain waveform of THz SHG from a DSTMS crystal (upper panel) and the corresponding THz pump waveform with a fundamental frequency of 1.6 THz (lower panel). (d) The time-domain waveform of THz SHG from an OH1 crystal (upper panel) and the corresponding THz pump waveform with a fundamental frequency of 0.8 THz (lower panel). (e)–(g) The frequency spectra of THz SHG from different crystals with incident THz waves at fundamental frequencies of 2.4, 1.6, and 0.8 THz.

both substantially higher than previous THz SHG studies. Similarly, the DSTMS crystal shows strong SHG at ~3.2 THz, as shown in Fig. 2(b), with a maximum conversion efficiency of 0.515% (the corresponding intensity conversion efficiency is 2.65×10^{-5}), which is unprecedented for this operating band. For low-frequency pump pulses of 0.8 THz, as shown in Fig. 2(c), the OH1 crystal demonstrates effective SHG with a maximum conversion efficiency of 0.049% (the corresponding intensity conversion efficiency is 2.40×10^{-7}), limited by the small pump electric field strength of 23.5 kV/cm. The resolution of the electric field strength of the second harmonics is affected by the background noise (refer to Sec. IV of Supplementary Material). Due to the weak second harmonics of 4.8 and 3.2 THz produced by the OH1 crystal [as shown in Figs. 2(a) and 2(b)] and 1.6 THz produced by DAST and DSTMS crystals [as shown in Figs. 2(c)], we provide a small number of valid measurements for subsequent mechanism analysis. Importantly, saturation of SHG is not observed within the range of the incident electric field, suggesting that there is still significant room for improvement in conversion efficiency. It is worth noting that prior to this study, only a few efforts had achieved conversion efficiencies of a similar magnitude based on the second-order nonlinearity of the material, and the operating frequency bands were all for low-frequency THz pump pulses below ~1 THz. For example, previous studies achieved a field conversion efficiency ($|E_{2f}|/|E_f|$) of ~0.035% for SHG in metamaterials excited by a 0.68 THz pulse with a maximum peak field of ~98.9 kV/cm,[30] and of ~0.3% in a superconductor pumped by a 0.5 THz pulse with a maximum peak field of ~21.7 kV/cm at a low temperature of ~4.2 K.[29]

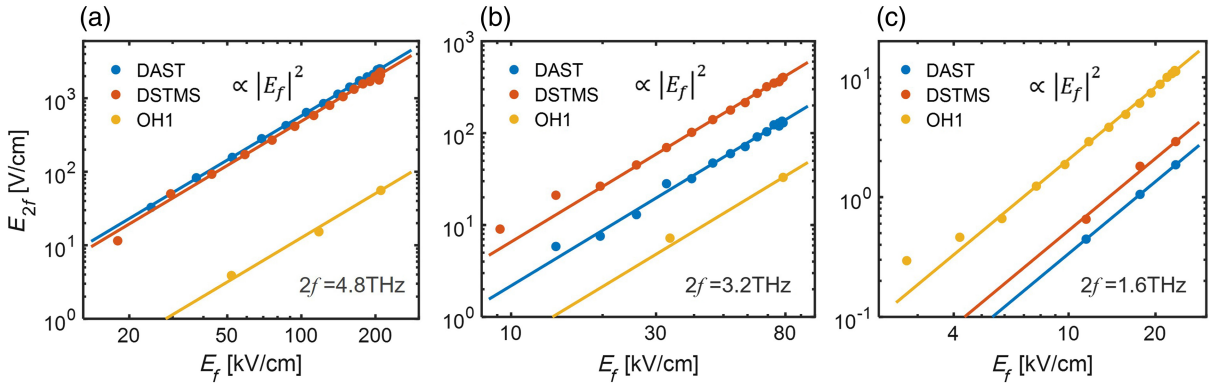

Fig. 2 The dependence of the generated second-harmonic field strength on the pump field strength. (a)–(c) The field strength of SHG from different crystals with the incident fundamental frequency of 2.4, 1.6, and 0.8 THz.

2.3 Influence of Dispersion and Phonon Absorption on SHG and Evaluation of Second-Order Nonlinear Susceptibility

To gain a deeper understanding of the physical mechanism behind strong SHG from organic crystals across a wide THz frequency range, we conducted a detailed analysis of various factors that affect SHG. The DAST, DSTMS, and OH1 crystals used in this study, which were commonly mentioned as THz sources in previous reports, exhibit absorption characteristics in the THz range that can significantly impact the spectra.[9,35] These absorption characteristics of the crystals in the THz range as well as the dispersion associated with refractive index perturbations mainly arise from phonon resonance, resulting in different frequency sensitivities of the three crystals to THz SHG. To analyze this complex process, we use the concept of effective distance [L_{eff}, refer to Eq. (3) in Appendix Sec. 4.2], which takes into account both dispersion and phonon absorption. The key parameters such as the refractive index and absorption coefficient of DAST, DSTMS, and OH1 crystals are depicted in Fig. S4 in the Supplementary Material, where they are simulated using the Lorentz model by considering the numerous resonant features of the different crystals.[37,41–45] The simulated effective distances L_{eff} for SHG at different fundamental frequencies in DAST, DSTMS, and OH1 crystals of varying thicknesses are shown in Figs. 3(a)–3(c). The fundamental pulses of 2.4, 1.6, and 0.8 THz selected in this study achieve optimal SHG conversion efficiency in different crystals, as shown in Figs. 2(a)–2(c), providing the necessary data for analyzing the influence of crystal phonon resonance on SHG. Specifically, DAST and DSTMS exhibit a pronounced phonon vibration near 1 THz, which is evident in the dip in the effective distance around ~1 THz in Figs. 3(a) and 3(b). This results in a low SHG when pumped by 0.8 THz, as shown in Fig. 2(c). However, DAST and DSTMS have a significant effective distance in the high-frequency region of 1.5 to 4.5 THz, leading to the strong SHG observed in Figs. 2(a) and 2(b). Moreover, the presence of a phonon vibration at ~3.1 THz in the DAST crystal directly inhibits SHG at 3.2 THz, distinguishing its frequency-doubling ability from that of DSTMS under 1.6 THz pumping conditions, as shown in Fig. 2(b). On the other hand, OH1 exhibits strong phonon vibrations at ~2.85 and ~4.5 THz, with high amplitude and damping. These vibrations strongly interfere with the dispersion and absorption of the crystal above 2 THz, resulting in difficulties in achieving SHG in the high-frequency range, as depicted in Figs. 2(a) and 2(b). This corresponds to a rapid decrease in the effective distance for the fundamental pulse above 1 THz, as shown in Fig. 3(c).

Furthermore, the thickness of DAST, DSTMS, and OH1 crystals selected in Figs. 1 and 2 are 300, 300, and 500 μm, respectively. Compared with the actual crystal thickness, the effective distance of organic crystals in the SHG process is limited by factors such as phase matching and absorption and is shown as a function of the operating frequency and crystal thickness [refer to Eq. (3) and Fig. 3]. Therefore, the simulations performed in Figs. 3(a)–3(c) also provide guidance for the thickness design and selection of crystal for SHG. Taking the DSTMS crystal as an example, the blue curves in Fig. 3(d) visually present the theoretical simulation of the effective distance with different crystal thicknesses at fundamental frequencies of 2.4, 1.6, and 0.8 THz. The simulated results show that DSTMS crystals in the thickness range of 100 to 300 μm have a high effective distance for THz pump pulses of these three frequencies. However, due to the difficult manufacturing process of organic crystal materials, the thickness of the thinnest DSTMS crystal we have commercially obtained is 300 μm. We further measured the electric field of SHG from DSTMS crystals with thicknesses of 300, 400, and 500 μm at three fundamental frequencies, as indicated by the red dots in Fig. 3(d). The results demonstrate that the measured electric field of SHG aligns with the trend of the effective distance curve, implying that the evaluation of effective distance can directly reflect the THz electric strength of SHG. This information is valuable in selecting the optimal crystal thickness for SHG at a specific pump frequency.

Based on the above series of theoretical analysis and experimental measurements, we further calculated the second-order nonlinear susceptibility $\chi^{(2)}$ of the crystal at different THz fundamental frequencies. The detailed calculation method is provided in Appendix Sec. 4.2. The relationship between the measured electric field of the second harmonics and the second-order nonlinear susceptibility $\chi^{(2)}$ can be described by Eq. (2), which takes into consideration various factors, such as dispersion, absorption, and the effective distance discussed earlier. As a result, we determine that the $\chi^{(2)}$ of the DAST crystal pumped at frequencies of 2.4, 1.6, and 0.8 THz are 1036, 1265, and 522 pm/V, respectively. Similarly, the measured $\chi^{(2)}$ of the DSTMS crystal pumped at frequencies of 2.4, 1.6, and

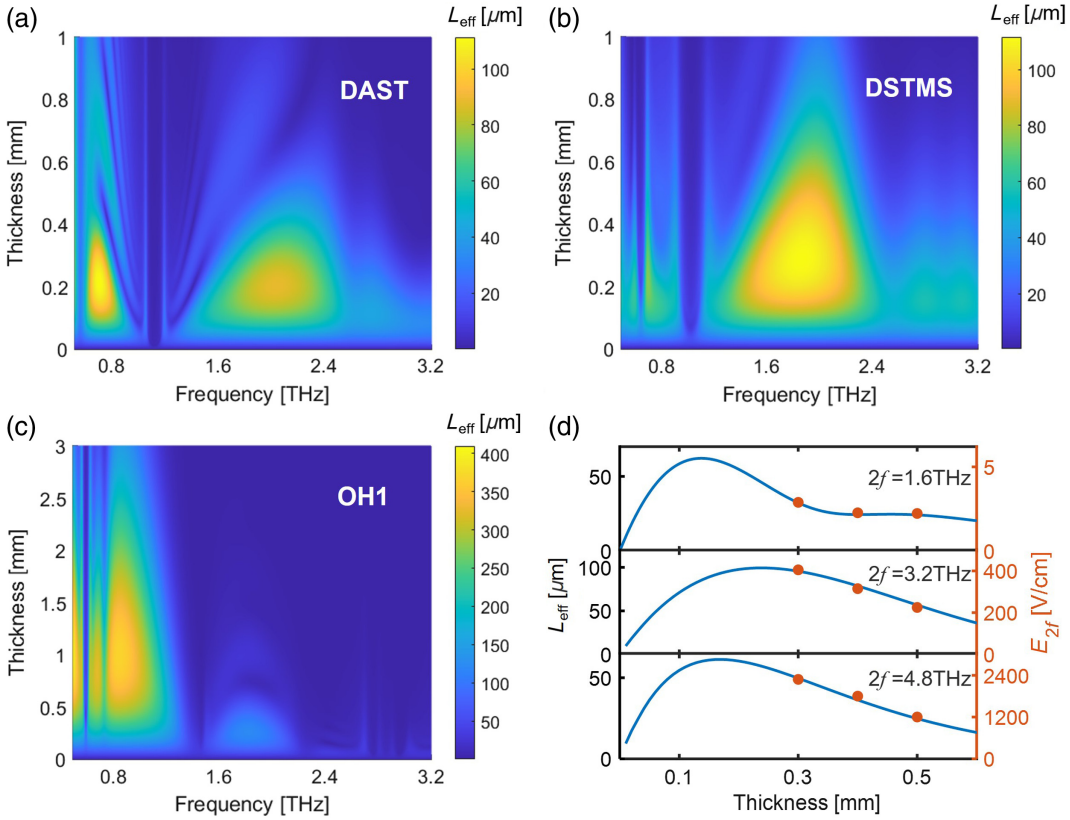

Fig. 3 The effective distance for SHG in crystals. (a)–(c) The effective distance for SHG in DAST, DSTMS, and OH1 crystals with varying thicknesses under different fundamental frequencies' pumping. (d) The blue curves depict the simulated effective distance for SHG in DSTMS crystals of varying thicknesses under fundamental frequencies of 2.4, 1.6, and 0.8 THz, and the red dots represent the measured electric fields of SHG from DSTMS crystals with thicknesses of 300, 400, and 500 μm under the three fundamental frequencies.

0.8 THz are 957, 961, and 521 pm/V, respectively. For the OH1 crystal, the $\chi^{(2)}$ at pump frequencies of 2.4, 1.6, and 0.8 THz are measured as 162, 136, and 130 pm/V, respectively.

2.4 Polarization Dependence of SHG in Crystals

Taking the DAST crystal as an example, the polarization dependence of SHG related to material anisotropy is further discussed. Assuming that the polarization direction of the fundamental pulse is in the x direction and is incident perpendicular to the crystal. φ represents the rotation angle of the a axis of the DAST crystal relative to the polarization direction of the fundamental wave (as shown in Fig. S1 of the Supplementary Material). We rotate the organic crystal DAST and measure the electric field components of SHG along the x and y directions using a GaP crystal and obtain the time-domain waveform of SHG with different rotation angles, as shown in Figs. 4(a) and 4(b). The bottom panels of the figure depict the maximum electric field strength of SHG from the crystal with a time delay of $t = 2$ ps, and the rotation angle of 0 deg represents the polarization direction of the incident pulse along the a axis of the DAST crystal. Based on the calculation of the polarizability tensor element in the crystal (see Appendix Sec. 4.3 for more details), the electric field measured along the x direction can be expressed as $E_x(2\omega) \propto 2(d_{11}E_0^2\cos^3\varphi + d_{12}E_0^2\sin^2\varphi\cos\varphi)$. Similarly, the electric field measured along the y direction can be expressed as $E_y(2\omega) \propto 2(d_{11}E_0^2\cos^2\varphi\sin\varphi + d_{12}E_0^2\sin^3\varphi)$, where $d_{ij} = \frac{1}{2}\chi_{ij}$ represents the nonlinear optical coefficients for THz SHG of the crystal.[40,46]

We find the SHG at the rotation angle of 90 deg in Fig. 4(b), that is, the SHG measured along the crystal a axis with the incident fundamental pulse along the crystal b axis, is almost 0. This is mainly due to the severe phase mismatch between the crystal a axis and b axis in the THz band and implies a small d_{12} component, which is further supported by our fitting results. We use functions $\cos^3\varphi$ and $\cos^2\varphi\sin\varphi$ to fit the measured electric fields in the x and y directions, respectively, as indicated by the red lines in the figure. The good agreement between the simulated curve and the measurement suggests that the contribution of d_{12} is negligible and can be disregarded. As a result, the main component contributing to SHG in DAST crystals is d_{11}, which represents the highest electro-optic tensor coefficient. This implies that the most efficient SHG occurs when the polarization of all beams is along the a axis of the DAST crystal. This value of d_{11}, as well as $\chi^{(2)}$, has not been experimentally reported in the THz band, but in our experiment, it can be approximately confirmed, i.e., $d_{11} \approx \frac{1}{2}\chi^{(2)}$. Specifically, we obtain the d_{11} values of DAST pumped at 2.4, 1.6, and 0.8 THz are ~518, 633, and 261 pm/V, respectively. In addition, we conducted simulations and measurements of the polarization

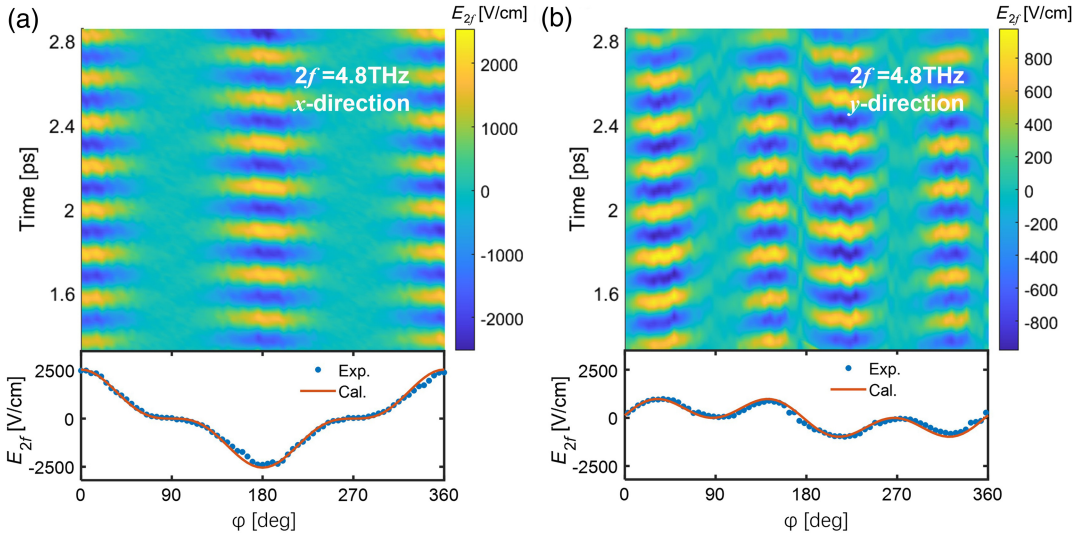

Fig. 4 Polarization dependence of SHG from DAST crystal at a pump frequency of 2.4 THz. (a), (b) The time-domain waveform of SHG measured in the *x* and *y* directions with the DAST rotation angle of φ. The color information represents the measured electric field strength of SHG. The bottom panels of the figure represent the variation of the peak electric field of the SHG with the rotation angle of φ.

characteristics of DSTMS and OH1 crystals, as shown in Figs. S5 and S6 in the Supplementary Material. These results also follow the same trend as DAST, confirming that the nonlinear component that plays a major role in THz SHG is d_{11} in the DSTMS crystal and d_{33} in the OH1 crystal, the latter due to the structural properties of the *a* cut of the OH1 crystal.[34,47–49] Our findings suggest that when DAST/DSTMS and OH1 crystals are used as THz frequency-doubling materials, the *a*-polarized pump and *c*-polarized pump of the respective crystals are preferred.

3 Discussion and Conclusion

Based on the theoretical simulations and experimental measurements discussed above, it can be concluded that the strong THz SHG observed in organic crystals can primarily be attributed to their high nonlinear polarization and low dispersion loss properties. The asymmetry of molecular structures in organic crystals, coupled with the uneven electron distribution caused by the presence of strong electron donors and acceptors, provides the conditions necessary for these organic crystals to exhibit strong second-order nonlinear coefficients. Moreover, the specific molecular structures and bonding patterns in these organic crystals form complex π-electron conjugated systems. The π-electrons in this conjugated system are not confined to a specific atom but are distributed across the atoms of the entire conjugated system,[33,34] supporting a broader distribution and movement of electrons, and a more sensitive response to electric fields, and the second-order nonlinear susceptibility be further enhanced. The π-electron system also possesses small energy gaps in its electronic energy levels, making it capable of absorbing and emitting photons in the THz frequency range. Notably, the three advanced crystals used in our study are designed as chromophores packed with their main charge transfer axis, leading to a high diagonal acentric order parameter, which is closely optimized for THz photonics applications,[33,37] thus resulting in enhanced second-order nonlinear effects.

Another significant factor contributing to the efficient SHG of organic crystals is their low dispersion losses in specific THz frequency ranges. For instance, DAST and DSTMS crystals exhibit refractive index differences of less than 0.1 within 2 to 6 THz range, while the OH1 crystal has a refractive index difference of less than 0.1 below 2 THz. These characteristics enable organic crystals to achieve coherence length (l_c) for SHG of over several hundred micrometers within the corresponding frequency band (>300 μm in DAST, >500 μm in DSTMS, and >1 mm in OH1), indicating that the THz fundamental and second-harmonic pulses are phase-matched during propagation through the selected crystal, while also establishing favorable conditions [refer to Eq. (3)] for effective distances required to generate second harmonics. Furthermore, we believe that phonon vibration has an effect on both the nonlinear polarizability and the effective distance of the SHG process in organic crystals, and the two effects show a competitive relationship. On the one hand, phonon vibration is an energy transfer process in the crystal structure, which indicates that organic crystals have a strong lattice effect at the THz scale and also enhances the sensitivity of π-electrons in the conjugated system to changes in the incident electric field, resulting in large second-order nonlinear susceptibility of organic crystals. On the other hand, phonon vibration causes dispersion and absorption of the crystal, which affects the effective distance for SHG. For example, the DAST crystal has a phonon mode near 3.1 THz, resulting in a larger second-order nonlinear susceptibility than the DSTMS crystal for SHG at 3.2 THz, but at the same time, this phonon vibration also leads to stronger dispersion and absorption, making the effective distance of the DAST crystal small. Under the above comprehensive influence, the SHG of DAST at 3.2 THz is weaker than that of DSTMS crystal. Therefore, we suggest that in future applications, the operating frequency range of organic crystals used as THz SHG devices should moderately avoid resonant sharp peaks of phonons. These findings can be extrapolated to various types of organic crystals in the THz field,

including N-Benzyl-2-methyl-4-nitroaniline (BNA),[50] 2-(4-hydroxy-3-methoxystyryl)-1-methylquinolinium 2,4,6-trimethylbenzenesulfonate (HMQ-TMS),[51] and potential future nonlinear optical crystals, thereby offering valuable theoretical guidance for selecting suitable crystal samples based on the desired operating frequency and the distribution of phonon resonance within the sample.

In summary, we introduced organic crystals as a novel category in the field of SHG over a wide THz range. By directly exciting the second-order nonlinear response in DAST, DSTMS, and OH1 crystals with three THz fundamental pulses at different frequencies, we observed effective SHG performance across a wide range of THz frequencies. Based on our findings, we recommend the OH1 crystal and DAST/DSTMS crystal as high-quality candidate materials for SHG with low- and high-frequency THz pulse pumping, respectively. Especially for high-frequency incident pulses of 2.4 THz, the conversion efficiency of the pumping harmonic field in DAST and DSTMS can exceed ~1%, marking a significant achievement. Similarly, for low-frequency pump pulses of 0.8 THz, the conversion efficiency can reach ~0.049%, which can be further optimized by increasing the thickness of the OH1 crystal and the strength of the pump electric field. Importantly, our results indicate that the SHG of three crystals does not saturate as the pump energy increases, suggesting that organic crystals have potential application prospects for generating extremely strong harmonics. Taking into account factors such as dispersion, phonon absorption, and polarization dependence, we further analyze the physical mechanism of SHG in these crystals and predict that DSTMS and DAST are suitable for higher-frequency bands beyond the measured range. Overall, the proposed THz SHG scheme based on organic materials is convenient, efficient, and has a wide operating frequency range, making it advantageous for material selection in artificial structure design and the development of small integrated devices. Furthermore, it opens up new opportunities for future nonlinear applications at THz frequencies.

4 Appendix

4.1 Experimental Setup

The THz time-domain spectroscopy employed in this experiment is based on the organic crystal pumped by a femtosecond laser with a repetitive frequency of 1 kHz for generating a strong-field THz wave. The setup of the experiment is illustrated in Fig. S1 in the Supplementary Material. The pump fundamental pulses of 2.4, 1.6, and 0.8 THz are selected by the specific type of THz bandpass filters and are vertically incident on the c-cut DAST crystal, c-cut DSTMS crystal, and a-cut OH1 crystal (Swiss Terahertz), respectively. A set of THz wire-grid polarizers are used to modulate the fundamental pump energy. The generated harmonics of 4.8, 3.2, and 1.6 THz are selected through the corresponding THz bandpass filters, and then measured using the EOS technique with a 1 mm thick ZnTe crystal or a 0.2 mm thick GaP crystal. The transmittance of different types of THz bandpass filters, as well as the response functions of ZnTe and GaP crystals to frequency, can be found in Fig. S2 in the Supplementary Material, which is used to correct the THz electric field values at different frequencies. Dry nitrogen gas is used to purge the system, eliminating the absorption of water vapor. More detailed information regarding the experimental setup can be found in the Supplementary Material.

4.2 Calculation of Second-Order Nonlinear Susceptibility and Effective Distance of Crystal for SHG

In the case of negligible absorption coefficient and near-perfect phase matching, the classical expression for the intensity of SHG in nonlinear media can be derived as[40,41,52]

$$I_{2\omega} = \frac{(2\omega)^2}{8c^3\varepsilon_0\varepsilon_\omega\sqrt{\varepsilon_{2\omega}}}|\chi^{(2)}|^2 l^2 I_\omega^2, \tag{1}$$

where $\chi^{(2)}$ is the second-order nonlinear susceptibility, and l is the sample thickness.

In our experiment, the crystal has a certain thickness, and the influence of dispersion and absorption on SHG cannot be ignored. Taking into account parameters such as the refractive index and absorption coefficient of the crystal, the amplitude of the electric field for THz SHG in the crystal can be expressed as[40,41,52]

$$|E_{2\omega}| = \frac{2\chi^{(2)}\omega^2 E_\omega^2}{\left[\frac{2\omega}{c}(n_{2\omega}+n_g)+i\left(\frac{\alpha_{2\omega}}{2}+\alpha_\omega\right)\right]c^2} L_{\text{eff}}(\omega, 2\omega, l), \tag{2}$$

where n_g is the optical group index of a fundamental THz pulse propagating within the sample. $\alpha_{2\omega}$ and α_ω represent the absorption coefficients of the sample for THz fundamental and second-harmonic pulses, respectively. $n_{2\omega}$ denotes the refractive index of the sample to the THz second-harmonic pulses. c denotes the vacuum speed of light. L_{eff} denotes the effective distance between the fundamental and second-harmonic pulse, which can be expressed as

$$L_{\text{eff}}(\omega, 2\omega, l) = \sqrt{\left\{\frac{\exp(-2\alpha_\omega l)+\exp(-\alpha_{2\omega} l)-2\exp[-(\alpha_\omega+\alpha_{2\omega}/2)l]\cos\left[\frac{\pi l}{l_c(\omega,2\omega)}\right]}{\left(\frac{\alpha_{2\omega}}{2}-\alpha_\omega\right)^2+\left[\frac{\pi}{l_c(\omega,2\omega)}\right]^2}\right\}}, \tag{3}$$

where $l_c(\omega, 2\omega) = \frac{\pi c}{\omega|n_{2\omega}-n_g|}$ represents the coherence length for SHG within the sample. Based on the absorption coefficient and refractive index for THz fundamental pulse and second-harmonic pulses (as shown in Fig. S4 of the Supplementary Material), the effective distance L_{eff} can be determined. By integrating the measurement of the harmonic electric field with the aforementioned equations, the second-order nonlinear susceptibility $\chi^{(2)}$ can be calculated.

4.3 Measurement of Nonlinear Optical Coefficients of the DAST Crystal for THz SHG

In this experiment, the polarization direction of the fundamental pulse is assumed to be in the x direction. The linearly polarized pump pulse propagates along the z direction (i.e., $E_z = E_{z'} = 0$), and it is incident on the sample perpendicularly. φ is the angle of crystal rotation relative to the x direction. The electric field components of the crystal can be expressed as $E_{x'} = E_0 \cos\varphi$, $E_{y'} = -E_0 \sin\varphi$, and $E_{z'} = 0$. The DAST crystal has a monoclinic structure, containing 10 nonzero second-order nonlinear polarizability tensors, and consequently, the relationship between the second-order polarization tensor matrix and the electric field component for SHG in DAST can be expressed as

$$\begin{bmatrix} E_{x'}(2\omega) \\ E_{y'}(2\omega) \\ E_{z'}(2\omega) \end{bmatrix} \propto 2 \begin{bmatrix} d_{11} & d_{12} & d_{13} & 0 & d_{15} & 0 \\ 0 & 0 & 0 & d_{24} & 0 & d_{26} \\ d_{31} & d_{32} & d_{33} & 0 & d_{35} & 0 \end{bmatrix} \begin{bmatrix} E_{x'}^2(\omega) \\ E_{y'}^2(\omega) \\ 0 \\ 0 \\ 0 \\ 2E_{x'}(\omega)E_{y'}(\omega) \end{bmatrix}. \tag{4}$$

So, the second-order electric field component in the crystal can be written as

$$\begin{aligned} E_{x'}(2\omega) &\propto 2[d_{11}E_{x'}^2(\omega) + d_{12}E_{y'}^2(\omega)] \\ &= 2(d_{11}E_0^2\cos^2\varphi + d_{12}E_0^2\sin^2\varphi), \\ E_{y'}(2\omega) &\propto 4d_{26}E_{x'}(\omega)E_{y'}(\omega) \\ &= -4d_{26}E_0^2\cos\varphi\sin\varphi. \end{aligned} \tag{5}$$

If the above electric field is projected onto the laboratory coordinates, the measured electric field is as follows:

$$\begin{aligned} E_x(2\omega) &= E_{x'}(2\omega)\cos\varphi - E_{y'}(2\omega)\sin\varphi \\ &\propto 2(d_{11}E_0^2\cos^3\varphi + d_{12}E_0^2\sin^2\varphi\cos\varphi) \\ &\quad + 4d_{26}E_0^2\cos\varphi\sin^2\varphi, \\ E_y(2\omega) &= E_{x'}(2\omega)\sin\varphi + E_{y'}(2\omega)\cos\varphi \\ &\propto 2(d_{11}E_0^2\cos^2\varphi\sin\varphi + d_{12}E_0^2\sin^3\varphi) \\ &\quad - 4d_{26}E_0^2\cos^2\varphi\sin\varphi, \end{aligned} \tag{6}$$

where d_{26} is not applicable in our experimental conditions and can be disregarded. In addition, the contribution of d_{12} is negligible, as discussed in the main text. Therefore, the main component contributing to SHG in DAST crystals is d_{11}, and it can be approximately confirmed as $d_{11} \approx \frac{1}{2}\chi^{(2)}$ in this work.

Disclosures

The authors declare no conflicts of interest.

Code and Data Availability

Data underlying the results presented in this paper are not publicly available at this time but may be obtained from the authors upon reasonable request.

Acknowledgments

This work was supported by the National Key R&D Program of China (Grant No. 2022YFB3806000), the National Natural Science Foundation of China (Grant Nos. 61935001, 62205020, 62205294, 52332006, 92163129, and U2241226), the China Postdoctoral Science Foundation (Grants Nos. 2022M710372 and 2022M710130), the Zhejiang Science and Technology Association young talent lifting project, and the Beijing Science and Technology Association young talent lifting project.

References

1. S. L. Rolston and W. D. Phillips, "Nonlinear and quantum atom optics," *Nature* **416**(6877), 219–224 (2002).
2. P. Knüppel et al., "Nonlinear optics in the fractional quantum Hall regime," *Nature* **572**(7767), 91–94 (2019).
3. J. Lee et al., "Giant nonlinear response from plasmonic metasurfaces coupled to intersubband transitions," *Nature* **511**(7507), 65–69 (2014).
4. A. von Hoegen et al., "Probing the interatomic potential of solids with strong-field nonlinear phononics," *Nature* **555**(7694), 79–82 (2018).
5. J. Bloch et al., "Strongly correlated electron-photon systems," *Nature* **606**(7912), 41–48 (2022).
6. L. Hu et al., "Quasi-BIC enhanced broadband terahertz generation in all-dielectric metasurface," *Adv. Opt. Mater.* **10**(12), 2200193 (2022).
7. L. Carletti et al., "Nonlinear THz generation through optical rectification enhanced by phonon–polaritons in lithium niobate thin films," *ACS Photonics* **10**(9), 3419–3425 (2023).
8. M. Fang et al., "Investigation of broadband terahertz generation from metasurface," *Opt. Express* **26**(11), 14241–14250 (2018).
9. M. Shalaby and C. P. Hauri, "Demonstration of a low-frequency three-dimensional terahertz bullet with extreme brightness," *Nat. Commun.* **6**(1), 5976 (2015).
10. B. Liu et al., "Generation of narrowband, high-intensity, carrier-envelope phase-stable pulses tunable between 4 and 18 THz," *Opt. Lett.* **42**(1), 129–131 (2017).
11. Z. Zhang et al., "Manipulation of polarizations for broadband terahertz waves emitted from laser plasma filaments," *Nat. Photonics* **12**(9), 554 (2018).
12. H. A. Hafez et al., "Extremely efficient terahertz high-harmonic generation in graphene by hot Dirac fermions," *Nature* **561**(7724), 507–511 (2018).
13. K. J. Tielrooij et al., "Milliwatt terahertz harmonic generation from topological insulator metamaterials," *Light Sci. Appl.* **11**(1), 315 (2022).
14. K. Fan et al., "Nonlinear terahertz metamaterials via field-enhanced carrier dynamics in GaAs," *Phys. Rev. Lett.* **110**(21), 217404 (2013).
15. H. R. Seren et al., "Nonlinear terahertz devices utilizing semiconducting plasmonic metamaterials," *Light Sci. Appl.* **5**(5), e16078 (2016).
16. H. J. Choi et al., "Control of terahertz nonlinear transmission with electrically gated graphene metadevices," *Sci. Rep.* **7**(1), 42833 (2017).
17. O. Schubert et al., "Sub-cycle control of terahertz high-harmonic generation by dynamical Bloch oscillations," *Nat. Photonics* **8**(2), 119–123 (2014).
18. D. Turchinovich, J. M. Hvam, and M. C. Hoffmann, "Self-phase modulation of a single-cycle terahertz pulse by nonlinear free-

carrier response in a semiconductor," *Phys. Rev. B* **85**(20), 201304 (2012).
19. P. Bowlan et al., "Ultrafast terahertz response of multilayer graphene in the nonperturbative regime," *Phys. Rev. B* **89**(4), 041408 (2014).
20. B. Cheng et al., "Efficient terahertz harmonic generation with coherent acceleration of electrons in the Dirac semimetal Cd_3As_2," *Phys. Rev. Lett.* **124**(11), 117402 (2020).
21. H. Linnenbank et al., "Second harmonic generation spectroscopy on hybrid plasmonic/dielectric nanoantennas," *Light Sci. Appl.* **5**(1), e16013 (2016).
22. Y. Tan et al., "Water-based coherent detection of broadband terahertz pulses," *Phys. Rev. Lett.* **128**(9), 093902 (2022).
23. X. C. Zhang, A. Shkurinov, and Y. Zhang, "Extreme terahertz science," *Nat. Photonics* **11**(1), 16–18 (2017).
24. M. S. Nikoo et al., "Nanoplasma-enabled picosecond switches for ultrafast electronics," *Nature* **579**(7800), 534–539 (2020).
25. Q. Li et al., "Subterahertz collective dynamics of polar vortices," *Nature* **592**(7854), 376–380 (2021).
26. J. Ma et al., "Security and eavesdropping in terahertz wireless links," *Nature* **563**(7729), 89–93 (2018).
27. A. Mayer and F. Keilmann, "Far-infrared nonlinear optics. I. $\chi(2)$ near ionic resonance," *Phys. Rev. B* **33**(10), 6954 (1986).
28. W. W. Bewley et al., "Far-infrared second-harmonic generation in $GaAs/Al_xGa_{1-x}$ As heterostructures: perturbative and nonperturbative response," *Phys. Rev. B* **48**(4), 2376 (1993).
29. C. Vaswani et al., "Terahertz second-harmonic generation from lightwave acceleration of symmetry-breaking nonlinear supercurrents," *Phys. Rev. Lett.* **124**(20), 207003 (2020).
30. Y. Wen et al., "A universal route to efficient nonlinear response via Thomson scattering in linear solids," *Natl. Sci. Rev.* **10**(7), nwad136 (2023).
31. S. R. Marder, J. W. Perry, and W. P. Schaefer, "Synthesis of organic salts with large 2nd-order optical nonlinearities," *Science* **245**, 626–628 (1989).
32. L. R. Dalton, P. A. Sullivan, and D. H. Bale, "Electric field poled organic electro-optic materials: state of the art and future prospects," *Chem. Rev.* **110**(1), 25–55 (2010).
33. L. Dalton et al., *Nonlinear Optical Properties of Organic Molecules and Crystals*, Cambridge University Press, Cambridge, United Kingdom (2015).
34. Z. Yang et al., "Molecular engineering of stilbazolium derivatives for second-order nonlinear optics," *Chem. Mater.* **19**(14), 3512–3518 (2007).
35. C. Ruchert, C. Vicario, and C. P. Hauri, "Spatiotemporal focusing dynamics of intense supercontinuum THz pulses," *Phys. Rev. Lett.* **110**(12), 123902 (2013).
36. C. Vicario, B. Monoszlai, and C. P. Hauri, "Single-cycle terahertz fields from a laser-driven large-size partitioned organic crystal," *Phys. Rev. Lett.* **112**(21), 213901 (2014).
37. M. Jazbinsek et al., "Organic crystals for THz photonics," *Appl. Sci.* **9**(5), 882 (2019).
38. K. M. Holland et al., "Characterization of organic crystals for second-harmonic generation," *Opt. Lett.* **48**(22), 5855–5858 (2023).
39. H. Zhao et al., "Ultrafast hydrogen bond dynamics of liquid water revealed by terahertz-induced transient birefringence," *Light Sci. Appl.* **9**(1), 136 (2020).
40. R. W. Boyd, *Nonlinear Optics*, Elsevier, Amsterdam (2003).
41. F. D. Brunner et al., "A hydrogen-bonded organic nonlinear optical crystal for high-efficiency terahertz generation and detection," *Opt. Express* **16**(21), 16496–16508 (2008).
42. P. D. Cunningham and L. M. Hayden, "Optical properties of DAST in the THz range," *Opt. Express* **18**(23), 23620–23625 (2010).
43. G. Montemezzani et al., "Running electric field gratings for detection of coherent radiation," *J. Opt. Soc. Am. B: Opt. Phys.* **32**(6), 1078–1083 (2015).
44. A. Majkic et al., "Terahertz source at 9.4 THz based on a dual-wavelength infrared laser and quasi-phase matching in organic crystals OH1," *Appl. Phys. Lett.* **105**(14), 141115 (2014).
45. M. Stillhart, A. Schneider, and P. Günter, "Optical properties of 4-N,N-dimethylamino-4-N -methyl-stilbazolium 2,4,6-trimethylbenzenesulfonate crystals at terahertz frequencies," *J. Opt. Soc. Am. B* **25**(11), 1914–1919 (2008).
46. M. Jazbinsek, L. Mutter, and P. Guenter, "Photonic applications with the organic nonlinear optical crystal DAST," *IEEE J. Sel. Top. Quantum Electron.* **14**(5), 1298–1311 (2008).
47. Z. Yang et al., "Large-size bulk and thin-film stilbazolium-salt single crystals for nonlinear optics and THz generation," *Adv. Funct. Mater.* **17**(13), 2018–2023 (2007).
48. O. P. Kwon et al., "Organic phenolic configurationally locked polyene single crystals for electro-optic and terahertz wave applications," *Adv. Funct. Mater.* **18**(20), 3242–3250 (2008).
49. S. J. Kwon et al., "Crystal growth and morphology control of OH1 organic electrooptic crystals," *Cryst. Growth Design* **10**(4), 1552–1558 (2010).
50. H. Zhao et al., "Efficient broadband terahertz generation from organic crystal BNA using near infrared pump," *Appl. Phys. Lett.* **114**(24), 241101 (2019).
51. A. Rovere et al., "Generation of high-field terahertz pulses in an HMQ-TMS organic crystal pumped by an ytterbium laser at 1030 nm," *Opt. Express* **26**(3), 2509–2516 (2018).
52. A. Schneider et al., "Generation of terahertz pulses through optical rectification in organic DAST crystals: theory and experiment," *J. Opt. Soc. Am. B* **23**(9), 1822–1835 (2006).

Hang Zhao received her PhD in instruments science and technology from Beijing Institute of Technology, Beijing, China, in 2021. She is currently working at the postdoctoral station of optical engineering of Beijing Institute of Technology. Her research interests include terahertz generation and detection.

Yong Tan received his PhD in instruments science and technology from Beijing Institute of Technology, Beijing, China, in 2021. He is currently working at the postdoctoral station of Yangtze Delta Region Institute, Tsinghua University, Jiaxing, China. His research focuses on terahertz metamaterials.

Chen Wang received her BS degree from Tsinghua University, Beijing, China, in 2018. She is currently pursuing her PhD in materials science and engineering at Tsinghua University. Her research focuses on nonlinear metasurfaces.

Ming Liu received his PhD in information-sensing technology and instruments from Beijing Institute of Technology, Beijing, China, in 2009. He is currently an associate professor at the School of Optoelectronics, Beijing Institute of Technology. His research interests include intelligent image analysis and machine vision based on deep learning and terahertz technology.

Yongzheng Wen is an associate professor of materials science and engineering at Tsinghua University. He received his BS degree from Sichuan University, Chengdu, China, in 2010 and his PhD from Peking University, Beijing, China, in 2015. His research interests include metamaterials, nonlinear optics, infrared and terahertz technologies, and micro/nano electromechanical systems. In recent years, he has published over 40 papers and presided over five national projects.

Yuejin Zhao received his PhD in optical engineering from Beijing Institute of Technology, Beijing, China, in 1990. He is currently a professor in the School of Optoelectronics, Beijing Institute of Technology. He has disciplinary responsibility as a team leader of "Instrument Science and Technology" at the Beijing Institute of Technology. His current research interests include terahertz imaging technology based on MEMS-infrared imaging technology, space-optical technology, and intelligent photoelectric instrument development.

Ji Zhou is a professor of materials science and engineering at Tsinghua University and an academician of the Chinese Academy of Engineering. He received his BS degree from Jilin University, Changchun, China, in 1983 and his PhD from Peking University, Beijing, China, in 1991. He has engaged in the research of metamaterials, photonic materials, as well as functional ceramic materials and devices. He has published over 400 papers and holds over 50 patents. He is the chairman of the academic committee of the State Key Laboratory for New Ceramics and Fine Processing, the chairman of the Metamaterial Branch of the Chinese Materials Research Society (C-MRS), and the chairman of the Science and Technology Committee of the China Electronic Components Industry Association.